

Impact of oxide bottom electrodes on resistive switching behavior associated with oxygen vacancy dynamics in Al/ZrO_2/BE ReRAM structures

Wei Zhang(张伟), Zhen Guo(郭震), Luobin Qiu(邱洛彬), Jun Liu(刘军), and Fangren Hu(胡芳仁)
Citation: Chin. Phys. B, 2025, 34 (**12**): 127303. DOI: 10.1088/1674-1056/ade4b2
http://cpb.iphy.ac.cn; http://iopscience.iop.org/cpb

What follows is a list of articles you may be interested in

Biodegradable and flexible *I*-carrageenan based RRAM with ultralow power consumption

Jing-Yao Bian(卞景垚), Ye Tao(陶冶), Zhong-Qiang Wang(王中强), Xiao-Ning Zhao(赵晓宁), Ya Lin(林亚), Hai-Yang Xu(徐海阳), and Yi-Chun Liu(刘益春)
Chin. Phys. B, 2024, 33 (**2**): 027301. DOI: 10.1088/1674-1056/ad19d4

Resistive switching behavior and mechanism of HfO_x films with large on/off ratio by structure design

Xianglin Huang(黄香林), Ying Wang(王英), Huixiang Huang(黄慧香), Li Duan(段理), and Tingting Guo(郭婷婷)
Chin. Phys. B, 2024, 33 (**1**): 017303. DOI: 10.1088/1674-1056/ad053a

Resistive switching properties of SnO_2 nanowires fabricated by chemical vapor deposition

Ya-Qi Chen(陈亚琦), Zheng-Hua Tang(唐政华), Chun-Zhi Jiang(蒋纯志), and De-Gao Xu(徐德高)
Chin. Phys. B, 2023, 32 (**9**): 097302. DOI: 10.1088/1674-1056/acc3fd

Review of resistive switching mechanisms for memristive neuromorphic devices

Rui Yang(杨蕊)
Chin. Phys. B, 2020, 29 (**9**): 097305. DOI: 10.1088/1674-1056/aba9c7

Charge transport and bipolar switching mechanismin a Cu/HfO_2/Pt resistive switching cell

Tingting Tan(谭婷婷), Tingting Guo(郭婷婷), Zhihui Wu(吴志会), Zhengtang Liu(刘正堂)
Chin. Phys. B, 2016, 25 (**11**): 117306. DOI: 10.1088/1674-1056/25/11/117306

Impact of oxide bottom electrodes on resistive switching behavior associated with oxygen vacancy dynamics in Al/ZrO_2/BE ReRAM structures

Wei Zhang(张伟)[1,†], Zhen Guo(郭震)[1], Luobin Qiu(邱洛彬)[1], Jun Liu(刘军)[1], and Fangren Hu(胡芳仁)[1,2,‡]

[1] *College of Electronic and Optical Engineering & College of Flexible Electronics (Future Technology), Nanjing University of Posts and Telecommunications, Nanjing* 210023, *China*

[2] *Peter Grunberg Research Center, Nanjing University of Posts and Telecommunications, Nanjing* 210003, *China*

(Received 15 April 2025; revised manuscript received 13 June 2025; accepted manuscript online 16 June 2025)

This study investigates the impact of oxide bottom electrode (BE) material and orientation on the resistive switching (RS) characteristics of Al/ZrO_2-based ReRAM devices. Devices with different oxide BEs, including (400)- and (222)-oriented ITO BEs deposited under pure argon and argon–oxygen (20% O_2) sputtering atmospheres, as well as $SrRuO_3$ (SRO), show distinct RS behaviors. The Al/ZrO_2/(400)-ITO and Al/ZrO_2/SRO devices demonstrate stable bipolar RS performance, with (400)-ITO enabling an abrupt reset process, a wider memory window ($> 10^4$), and superior stability, while SRO devices exhibit gradual reset transitions with lower power consumption. Furthermore, the crystallographic orientation control applied to ITO BE significantly affects the V_O dynamics and RS performance, with (222)-ITO devices exhibiting irreversible RS behavior. It is irrefutable that BE material and its orientation can strongly influence RS performance by modulating the V_O dynamics, electric field distribution, and conductive filament behavior. These findings underscore the importance of BE properties in optimizing ReRAM performance and provide valuable guidance for the development of high-efficiency memory devices.

Keywords: ZrO_2 film, resistive switching mechanism, electrode material and crystallographic orientation, oxygen vacancy dynamics

PACS: 73.40.Rw, 77.55.–g, 72.20.–i, 71.55.–i

DOI: 10.1088/1674-1056/ade4b2 **CSTR:** 32038.14.CPB.ade4b2

1. Introduction

The increasing demand for energy-efficient, high-density memory technologies to support advanced applications such as artificial intelligence (AI), the internet of things (IoT), and edge computing has positioned resistive random access memory (ReRAM) as a leading contender for next-generation non-volatile memory (NVM) devices.[1–7] ReRAM's simple metal–insulator–metal (MIM) pattern offers exceptional scalability, CMOS compatibility, low power consumption, and multi-functionality.[4,7,8] Unlike conventional memory technologies such as dynamic random-access memory (DRAM) and flash memory, which face scaling and performance limitations, ReRAM leverages resistive switching (RS) phenomena in oxide materials to achieve tunable electrical conductivity. This makes it particularly promising for ultra-dense storage and computation-in-memory architectures.[9] RS behavior in ReRAM devices is categorized into electrochemical metallization memory (ECM) and valence change memory (VCM), with the latter standing out for its stable bipolar RS characteristics, durability, and potential for NVM applications.[7,10] The performance of VCM-based ReRAM is predominantly dictated by the insulating oxide layer and electrode materials, which significantly affect oxygen vacancy (V_O) dynamics and interfacial behaviors.[11–14]

Among the various metal oxides employed as switching materials in VCM-based devices, zirconium dioxide (ZrO_2) has gained considerable attention for its wide bandgap (∼5 eV–7 eV), superior dielectric property, outstanding thermal and chemical stability, tunable defect chemistry and phase structure, high integration density, and non-destructive readout capability.[15–17] Compared to other commonly used oxides such as HfO_2 and TaO_x, ZrO_2 exhibits a lower leakage current and superior interface compatibility, which are beneficial for achieving high ON/OFF ratios and stable device operation.[18,19] Its robust intrinsic physical properties make ZrO_2 a promising candidate for RS applications, offering remarkable endurance and data retention essential for reliable memory performance.[17,20] In addition, ZrO_2 facilitates stable V_O migration pathways with moderate activation energy, enabling the controlled formation and rupture of conductive filaments (CFs) crucial for data storage.[21] Despite these advantages, the practical application of ZrO_2 in RS devices faces

†Corresponding author. E-mail: chanway@njupt.edu.cn

‡Corresponding author. E-mail: hufr@njupt.edu.cn

© 2025 Chinese Physical Society and IOP Publishing Ltd. All rights, including for text and data mining, AI training, and similar technologies, are reserved.

challenges, such as achieving uniform switching behavior and mitigating variability in V_O dynamics. These issues often stem from its high crystallization energy and the difficulty of precisely controlling V_O distribution under electrical stress.[3,22] To address these limitations, researchers have explored strategies such as doping with transition metals to stabilize V_O pathways, introducing multilayer or nanocomposite structures to improve switching stability, optimizing fabrication techniques or electrode properties to enhance film uniformity and interface quality.[16,20,23–27] However, the effectiveness of these methods depends significantly on the electrode–oxide interface, which directly influences V_O generation, migration, and recombination.

In this work, we aim to tailor the RS performance of Al/ZrO_2-based ReRAM devices by investigating the role of the bottom electrode (BE) interface configuration. Two distinct conductive oxides were employed as BEs: indium tin oxide (ITO), a transparent conductive oxide with tunable electrical and interfacial properties via deposition conditions and controllable crystallographic orientations ((400) and (222)); and $SrRuO_3$ (SRO), a metallic oxide featuring high electrical conductivity, structural compatibility with perovskite-type oxides, and the ability to form high-quality interfaces with ZrO_2. By systematically investigate the oxide–oxide interfaces formed by these materials, we examined their intrinsic properties' effects on interfacial charge transport characteristics, electric field distribution, and CF dynamics. Furthermore, we demonstrated the role of crystallographic orientation engineering in RS dynamics. This dual approach sheds light on the design principles for high-performance ReRAM devices.

2. Experimental details

All thin films were deposited using a multi-target magnetron sputtering system, with a base vacuum of 2.0×10^{-4} Pa. As shown in Fig. 1(a), mirror-polished (100) single crystalline Si substrates (10 mm×10 mm×0.5 mm) were used as the substrates. These substrates were cleaned sequentially by ultrasonic treatment in acetone, ethanol, and deionized water before being loaded into the vacuum chamber. The BE layers of ITO and SRO were sputtered from their respective ceramic targets with identical compositions using radio-frequency magnetron sputtering (RFMS). The crystallinity of the sputtered films was significantly influenced by the RFMS process parameters. Specifically, the crystallographic orientation of the ITO electrode varied with the oxygen partial pressures in the deposition atmosphere.

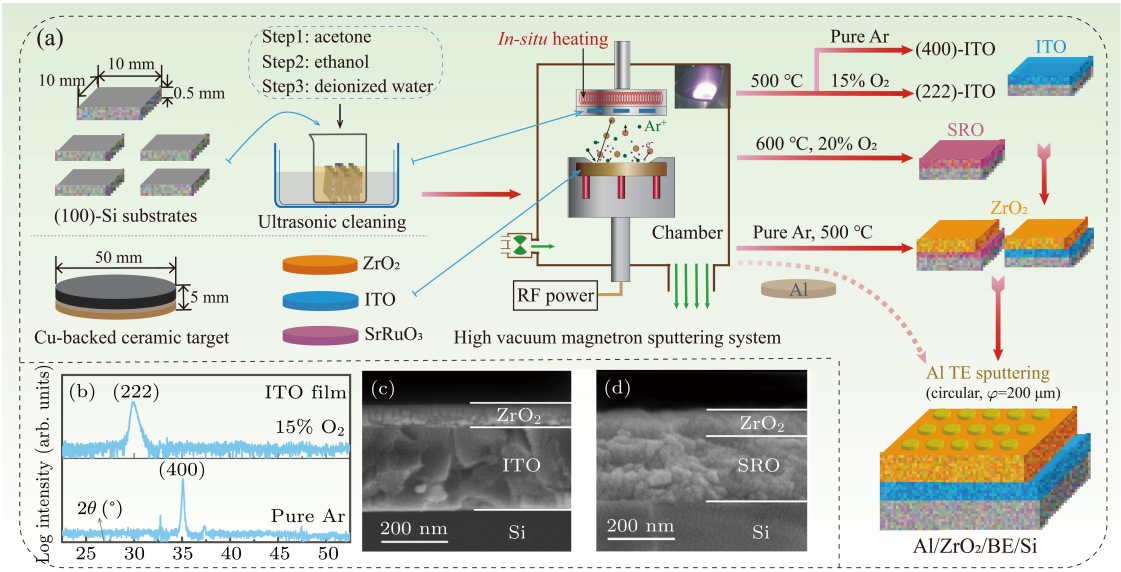


Fig. 1. (a) Fabrication process flow for Al/ZrO_2/BE(ITO,SRO)/Si ReRAM devices, and schematic illustration of the Al/ZrO_2/BE/Si device structure, (b) XRD patterns of ITO films deposited under different Ar/O_2 gas atmospheres, (c) and (d) cross-sectional images of ZrO_2/SRO/Si and ZrO_2/ITO/Si heterostructures, respectively.

As illustrated in Fig. 1(b), the ITO BE layer deposited in a pure Ar atmosphere exhibited a pronounced (400) preferential orientation. In contrast, when deposited in an oxygen–argon mixture containing 15% O_2, the ITO BE layer displayed a dominant (222) preferential orientation. Subsequently, an approximately 75-nm-thick ZrO_2 film was directly deposited onto the surface of the BE surface (a small portion was exposed by masking to facilitate electrical performance testing) from a ZrO_2 ceramic target using RFMS. The SEM cross-sectional images of the ZrO_2 heterostructures with two different oxide BE structures are shown in Figs. 1(c) and 1(d), respectively. Finally, circular Al top electrodes (TE) with a 200-μm-diameter array were deposited onto the ZrO_2 film layer using a metal shadow mask, forming an oxide–semiconductor–metal (OSM) structure on Si (Al/ZrO_2/BE/Si). All sputtering targets were cylindrical ($\Phi = 50$ mm, $h = 5$ mm) with a purity

of 99.99%. The specific deposition parameters for each film layer are detailed in Fig. 1(a).

The RS performance of these OSM structures was analyzed using a Keithley 4200 semiconductor characterization system in DC voltage sweeping mode. During testing, all operating voltages were applied to the TE, while the BE was kept grounded, with a current compliance (CC) of 1 mA to prevent device breakdown. Additionally, the cross-sectional images of the ZrO_2/BE/Si were analyzed using a field emission scanning electron microscope (FESEM, SU8000, Hitachi). The measured thicknesses of the ITO and SRO BE layers were approximately 250 nm and 180 nm, respectively (Figs. 1(c) and 1(d)). The crystallographic orientations of the ITO BE layers were characterized by x-ray diffractometer (XRD, Bruker D8 Advanced) using Cu-$K\alpha$ radiation. All measurements were conducted at room temperature.

3. Results and discussion

Figures 2(a)–2(c) present the typical current–voltage (I–V) characteristics of Al/ZrO_2/BE devices with different BEs under a voltage sweep sequence of $0 \rightarrow +V_{max} \rightarrow 0 \rightarrow -V_{max} \rightarrow 0$ V. A compliance current (CC) of 1 mA was applied during the positive voltage sweep to prevent permanent breakdown of the device. The thin lines denote multiple switching cycles, while the bold curve highlights a representative switching behavior for clarity. Device utilizing (400)-ITO and SRO as BEs both exhibit standard bipolar RS. During the set process, the device transitions from a high-resistance state (HRS) to a low-resistance state (LRS), driven by the formation of CFs through the migration and aggregation of V_Os. The reset process reverses this transition by rupturing CFs, thereby restoring the HRS and enabling repeatable RS cycles. However, the reset dynamics differ markedly between the two devices. The (400)-ITO device exhibits an abrupt reset process, characterized by a sharp current drop at a critical voltage, indicative of sudden CF rupture. In contrast, the SRO-based device undergoes a gradual LRS-to-HRS transition, beginning at a $V_{reset-begin}$ (≈ -0.4 V) and progressively increasing in resistance until the HRS is fully established at $V_{reset-stop}$ (≈ -1.3 V), as shown in Fig. 2(b). This gradual transition suggests a stepwise dissolution or dispersion of CFs over an extended voltage range.

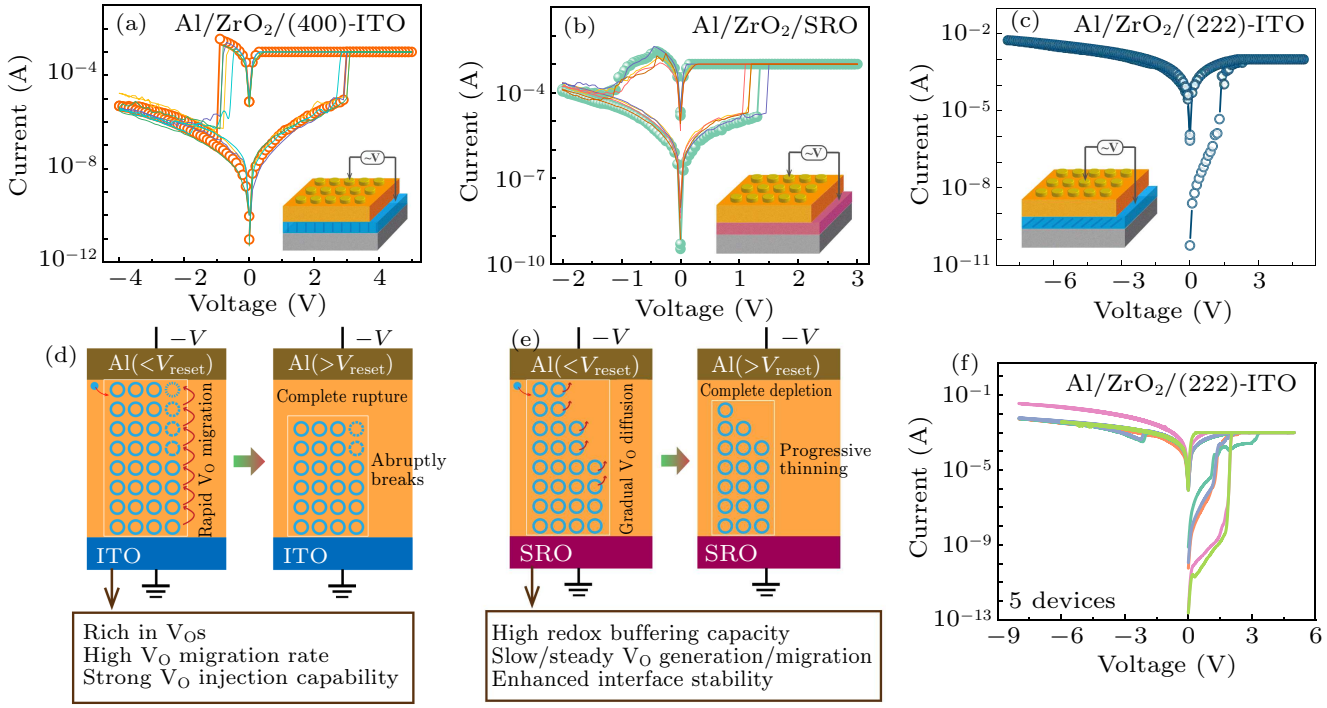


Fig. 2. (a)–(c) Typical set–reset I–V characteristics of Al/ZrO_2-based devices with different BEs. (d)–(e) Schematic illustrations of the reset mechanism, highlighting V_O dynamics in the Al/ZrO_2/(400)-ITO and Al/ZrO_2/SRO devices, respectively. (f) I–V characteristics of five randomly selected units of the Al/ZrO_2/(222)-ITO device.

The difference between these two structures arise from the distinct material properties and interfacial effects of the BEs, as schematically illustrated in Figs. 2(d) and 2(e). The V_O-rich ITO electrode, fabricated in a pure Ar atmosphere,[28] facilitates rapid V_O exchange and migration within the ZrO_2 layer. Upon application of the reset voltage, V_Os are swiftly driven by the strong electric field, triggering a fast and localized rupture of the CF, which results in the formation of a completely disconnected insulating region. In contrast, the SRO electrode, deposited in a 20% O_2 environment (Fig. 1(a)), possesses stronger redox buffering capabilities and exhibits lower V_O concentration and mobility. This leads to a more

controlled redistribution of V_Os, where CF rupture becomes partially diffusion-limited.[29] Under a negative bias, the gradual depletion of V_Os causes the CF to progressively thin and diffuse, ultimately leading to a smoother and more gradual CF breakdown. Additionally, the interfacial electric field distribution plays a crucial role in these differences. The (400)-ITO likely enhances localized electric field at the interface due to its defect structure and high conductivity, thereby accelerating CF rupture. Conversely, the SRO yields a more uniform field distribution, which further supports the gradual reset transition.

Interestingly, devices using (222)-oriented ITO as the BE show no reset behavior. As shown in Fig. 2(c), although the set process successfully induces an LRS, the device fails to return to the HRS. This behavior is attributed to the high grain boundary (GB) density in (222)-ITO, which leads to non-uniform V_O distributions and localized V_O accumulation near GBs. These GBs serve as V_O traps, forming robust conductive paths that are difficult to rupture. Consequently, the reverse voltage becomes insufficient to break these CFs, resulting in permanent LRS and the loss of RS functionality. All five randomly tested devices, which were subjected to identical voltage sweep conditions, exhibited similar behavior, as shown in Fig. 2(f)). Specifically, only the initial 'write' operation was succeeded, while subsequent 'erase' operations consistently failed. This RS failure could also be attributed to localized electric field intensification caused by the complex crystal plane structure, which may lead to charge accumulation or local breakdown.

To investigate the carrier transport mechanisms, figure 3(a) shows the $\log(I)$–$\log(V)$ curves during the set process for devices with (400)-ITO and SRO BEs. Both exhibit linear behavior in the LRS with slopes near 1 (0.95 and 0.94), indicative of Ohmic conduction dominated by V_O trapping at low voltages.[30,31] This conduction behavior suggests minimal energy dissipation, favoring low-power operation. In the HRS, the SRO device exhibits a slope of 1.37, suggesting that the carrier transport is influenced to some extent by space-charge accumulation, deviating from Ohm's law and indicating a space-charge limited current (SCLC) mechanism. However, the (400)-ITO device exhibits a two-segment behavior with slopes of 2.28 and 3.30 in the low- and high-voltage regions, respectively. This nonlinearity is characteristic of trap-related SCLC conduction, where carrier transport is affected not only by space-charge effects but also by trap states within the dielectric. Particularly in the high-voltage region, carriers may acquire sufficient energy to overcome these trap barriers, resulting in a rapid current increase. Such trap-filled SCLC behavior typically leads to nonlinear and voltage-sensitive current responses, potentially increasing power consumption at elevated operating voltages. From the fitted slopes, it is evident that the (400)-ITO device exhibits much higher slopes compared to the SRO device, indicating that its current increases more rapidly with voltage in the HRS. This behavior is closely related to the V_O properties of the electrodes, as V_O plays a crucial role in trap-assisted conduction.[14]

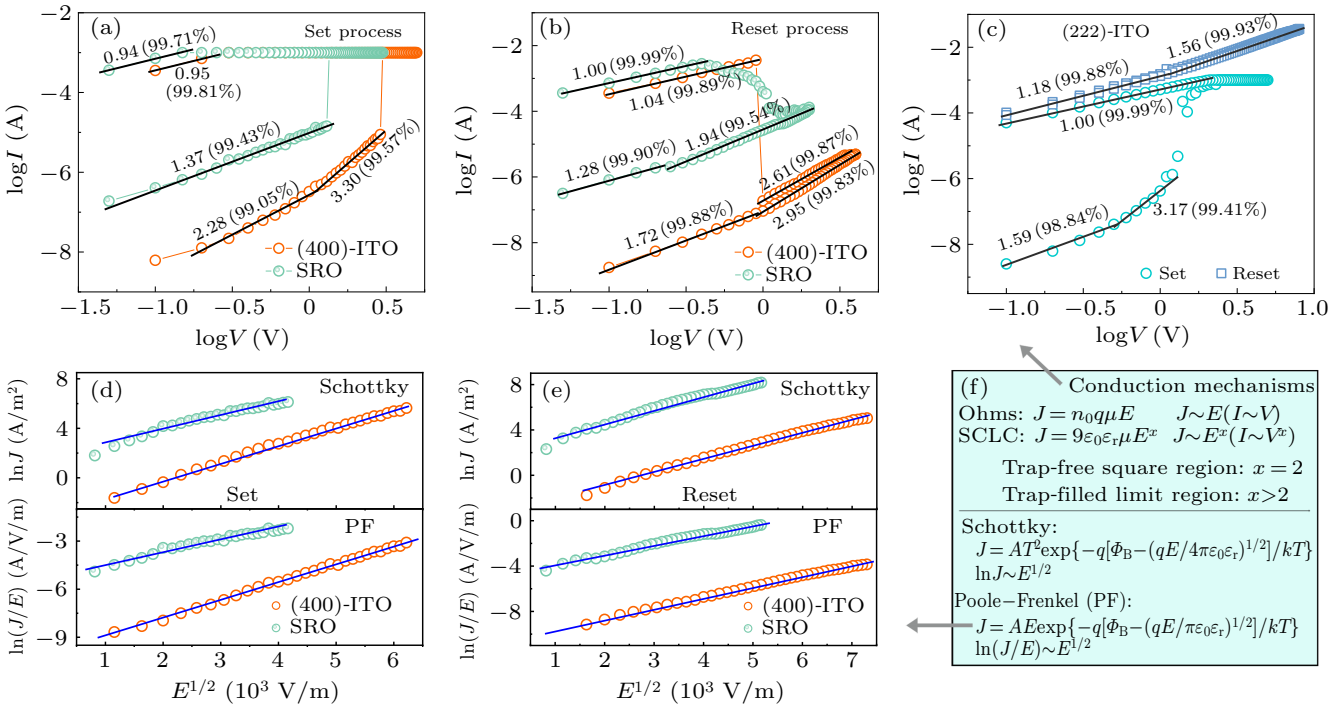


Fig. 3. Representative $\log I$–$\log V$ plots for (a) the set process and (b) the reset process of (400)-ITO and SRO BE devices. (c) Fitted $\log I$–$\log V$ curves for both set and reset processes of the (222)-ITO device. I–V curve fitting based on Schottky and PF emission mechanisms in the HRS during (d) the set process and (e) the reset process. (f) Expressions of current conduction mechanisms.

As previously mentioned, the (400)-ITO BE fabricated in pure Ar, is V_O-rich with a high V_O migration rate, unlike the SRO electrode, deposited in a 20% O_2 atmosphere. This high V_O mobility enables V_O to rapidly migrate and redistribute within the ZrO_2 film when a voltage is applied. The fast migration of V_O accelerates the injection of charge carriers and the accumulation of space-charge in the ZrO_2 layer, leading to localized conductivity changes and a rapid increase in current until the limiting current value is reached, as traps become filled, particularly at higher voltages.[32,33] Additionally, V_O redistribution can form more conductive channels in localized regions, further accelerating the current increase. As shown in Fig. 3(b), the reset process follows a similar conduction mechanism: Ohmic conduction in the LRS and SCLC in the HRS (with linear fitting coefficients of determination exceeding 99%). The conduction behavior of the (222)-ITO BE device in Fig. 3(c) further supports this trend: its set process resembles that of the (400)-ITO BE device, while its non-resistive reset process is SCLC-dominated.

In addition to the SCLC mechanism, Schottky emission (SE) phenomena are also commonly observed in ZrO_2-based ReRAM devices.[34–36] The SE current can be expressed as[37]

$$J = AT^2 \exp\left\{-q\left[\Phi_B - (qE/4\pi\varepsilon_0\varepsilon_r)^{1/2}\right]/kT\right\}.$$

This implies that if the device current follows the SE current, the relationship between $\ln J$ and $E^{1/2}$ should be linear. As shown in Fig. 3(d), the HRS current during the set process of both (400)-ITO and SRO BE devices follows the aforementioned linear relationship, indicating that the current transport process in our ZrO_2-based OSM structure is influenced by the SE mechanism. A similar result is observed for the reset process (Fig. 3(e)). Since SE occurs at the electrode/oxide interface, this implies that interface engineering plays a crucial role in improving device reliability. Additionally, under a strong electric field, Poole–Frenkel (PF) emission may also occur, where trapped electrons gain enough energy to be excited into the conduction band of the oxide. The high electric field lowers the Coulomb potential barrier, facilitating the thermal excitation of electrons from the traps. As illustrated in Fig. 3(f), the PF expression takes a form similar to that of SE, with the key distinction being that in the PF model, Φ_B refers to the depth of the trap potential well, whereas in SE, it corresponds to the height of the barrier. Moreover, due to the immobility of positive charges, the barrier lowering effect in PF emission is twice as strong as that observed in SE model.[37] As shown in Figs. 3(d) and 3(e), for the HRS current of both bipolar RS devices, $\ln J/E$ exhibits a clear linear relationship with $E^{1/2}$ indicating that both devices experience PF emission. Such conduction suggests deep trap states that require strong electric fields, potentially increasing energy input and local Joule heating, which may accelerate defect migration and reduce endurance. In summary, the HRS current conduction in our ZrO_2 devices is mainly governed by a combination of SE and PF mechanisms, especially under high electric fields. The ITO and SRO oxide BEs lower the Schottky barrier through interaction with the ZrO_2 layer, enabling electron flow via SE. Meanwhile, the strong electric field excites defect states within the ZrO_2 layer, providing electron capture sites triggering PF emission.

Figure 4(a) presents a comparison of the dc cycle switching endurance of (400)-ITO and SRO electrode devices for more than 500 cycles under a read voltage of 0.1 V, demonstrating stable resistance states for both devices. The values of the LRS resistance (R_{LRS}) for both are nearly identical ($\sim 300\ \Omega$). However, the HRS resistance (R_{HRS}) of the (400)-ITO device is consistently an order of magnitude higher than that of the SRO device, resulting in a memory window ~ 10 times larger, with average switching ratios reaching 3.6×10^4 and 2.1×10^3, respectively, as illustrated in the box plot in Fig. 4(b). A higher RHRS generally correlated with an increased set voltage (V_{set}) in ReRAM devices.[38] As shown in Fig. 4(b), the switching voltages of the ITO device are uniformly higher than those of the SRO device. The rapid migration and redistribution of V_Os facilitated by (400)-ITO require higher voltages for CF formation and rupture, thereby increasing V_{set} and V_{reset}. Conversely, the moderated V_O dynamics and uniform electric field distribution in SRO, coupled with its redox stability, promote CF formation and dissolution at lower voltages. Despite the lower R_{HRS}/R_{LRS} ratio of the SRO device, it remains well above practical application thresholds, providing a balance between memory performance and reduced power consumption.

Figure 4(c) depicts the cumulative distribution of R_{HRS} and R_{LRS} for ZrO_2-based ReRAM devices with (400)-ITO and SRO BEs. The figure also presents the statistical variables: mean (μ), standard deviation (σ), and coefficient of variation (σ/μ). For the (400)-ITO device, the LRS exhibits $\mu = 303.3\ \Omega$ with $\sigma/\mu = 0.24$, indicating stable CF formation, while the HRS has $\mu = 19\ \text{M}\Omega$ and $\sigma/\mu = 1.12$, reflecting greater variability due to the stochastic nature of V_O migration and redistribution, particularly during CF rupture under localized electric field. The SRO device features an LRS with $\mu = 344.3\ \Omega$ and $\sigma/\mu = 0.42$, indicating less consistent CF pathways compared to the (400)-ITO. Its HRS, with $\mu = 2.1\ \text{M}\Omega$ and a high σ/μ of 3.29, suggests considerable fluctuations, likely due to SRO's redox stability and uniform electric field distribution, which reduce abrupt V_O clustering but contribute to unpredictable CF dissolution. Figure 4(d)

confirms that both devices maintain good data retention up to 10^4 s, with only minor HRS degradation in the SRO device. Overall, (400)-ITO devices exhibit higher LRS stability through efficient V_O dynamics, while the greater HRS variability reflects CF rupture complexity. Thus, (400)-ITO provides a wider memory window and consistent performance, whereas SRO balances switching reliability with lower power consumption, favoring energy-efficient applications.

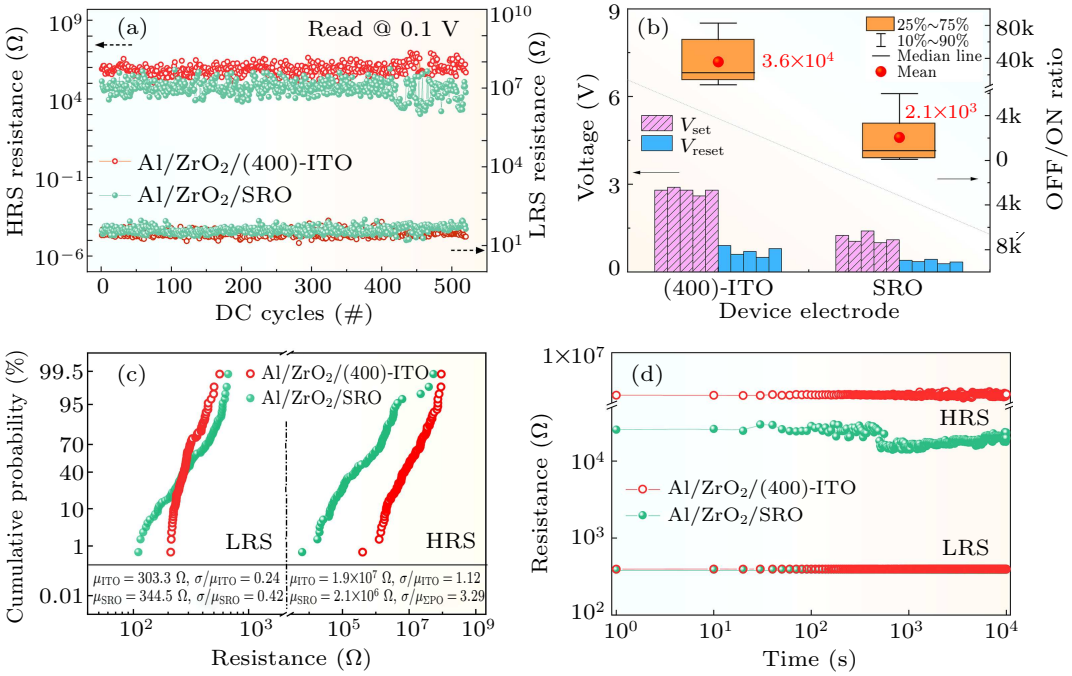


Fig. 4. RS characteristics of the Al/ZrO_2/(400)-ITO and Al/ZrO_2/SRO bipolar RS devices: (a) dc cycle switching endurance. (b) V_{set} and V_{reset} for multiple cycles, along with boxplots showing the distribution and mean values of the OFF/ON ratio. (c) Cumulative probability of R_{HRS} and R_{LRS}, with corresponding distribution parameters. (d) Retention properties.

To evaluate device-to-device stability, we randomly selected six units from each type of ZrO_2-based ReRAM (6 device units $\times$100 cycles). Figures 5(a) and 5(b) depict the average set and reset voltages ($\bar{V}_{set}$ and $\bar{V}_{reset}$) for individual units of the (400)-ITO and SRO electrode devices, respectively. The relatively small variations in $\bar{V}_{set}$ and $\bar{V}_{reset}$ among units within the same device type indicate good device-to-device stability for both ReRAM configurations, which is crucial for large-scale integration and commercial applications. A notable observation is that the $\bar{V}_{set}$ and $\bar{V}_{reset}$ values of the SRO-based devices are consistently lower than those of the (400)-ITO devices, suggesting that SRO BEs contribute to lower operating voltages and reduced power consumption. This difference can likely be attributed to the superior metallic nature of SRO, which facilitates more efficient charge injection and transport at the electrode/oxide interface. Furthermore, the closer $\bar{V}_{set}$ and $\bar{V}_{reset}$ values in the SRO-based devices indicate more uniform CF dynamics during the switching process. This uniformity may stem from the stronger metallic properties of SRO,[39] which lead to a more balanced interfacial behavior under both positive and negative bias. In the Al/ZrO_2/SRO configuration, the high conductivity and work function of SRO enable more symmetric charge carrier injection and V_O migration, thereby promoting a more consistent formation and dissolution of CFs. In contrast, the Al/ZrO_2/ITO structure exhibits more asymmetric interfacial behavior due to the semiconductor nature of ITO, which influences the CF dynamics and leads to greater variability in switching voltages.

Figures 5(c) and 5(d) illustrate the distribution (boxplot) of R_{HRS} and R_{LRS} values for individual device unit in both structures. The (400)-ITO devices generally exhibit lower box heights compared to SRO devices, indicating superior temporal stability, meaning that the resistance states remain more consistent over repeated switching cycles. Additionally, the narrower R_{HRS} distribution across different (400)-ITO device units suggests slightly better spatial stability, meaning that different units within the same device type exhibit less variability in their resistance states. This improved stability could be attributed to the highly oriented (400) texture of the ITO BE, which provides a more controlled interface for V_O migration and CF formation. In contrast, the broader R_{HRS} distribution in SRO-based devices suggests greater device-to-device variability, likely due to differences in how SRO interacts with V_Os. The strong metallic nature of SRO may lead to less constrained CF rupture dynamics, increasing variability in the HRS. Overall, from a device-to-device perspective, these results further confirm that (400)-ITO electrodes offer enhanced switching performance and stability, whereas SRO electrodes provide a favorable balance of lower power consumption and reliable switching behavior. These complementary characteristics suggest application-specific tradeoffs in designing ReRAM devices with optimized performance.

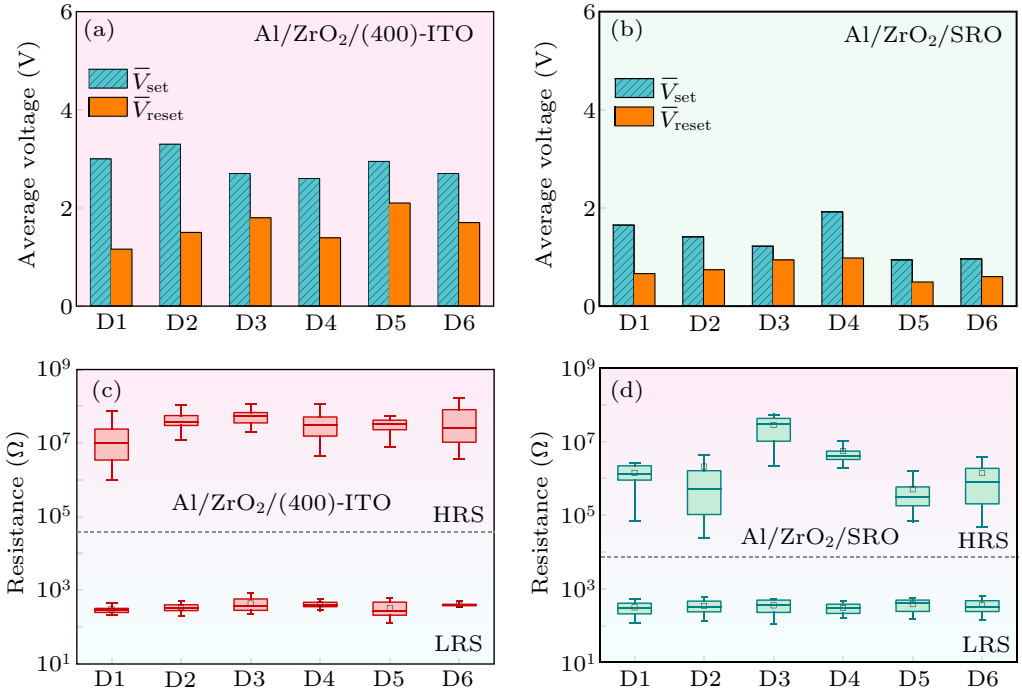


Fig. 5. Spatial variations for two Al/ZrO_2-based bipolar RS devices: (a)–(b) average set and reset voltages, and (c)–(d) boxplots of R_{HRS} and R_{LRS} distributions.

4. Conclusions

In this work, we comprehensively investigated the RS characteristics of Al/ZrO_2-based ReRAM devices employing (400)-ITO, (222)-ITO, and SRO as BEs. The results demonstrate that BE material properties critically influence V_O dynamics, electric field distribution, and CF behavior, thereby shaping RS performance. Devices with (400)-ITO and SRO electrodes demonstrated stable bipolar RS behavior with distinct reset mechanisms: (400)-ITO devices exhibited an abrupt reset process, while SRO devices displayed a gradual reset transition. The (400)-ITO devices achieved a larger memory window (3.6×10^4, $\sim 10\times$ that of SRO: 2.1×10^3) and superior temporal and spatial stability, whereas SRO devices offered reliable RS performance with lower power consumption. In contrast, devices with (222)-ITO BEs exhibited irreversible RS behavior due to non-uniform V_O distribution and aggregation at GBs or local breakdown. These findings emphasize the critical role of BE properties in optimizing RS behavior, offering valuable guidance for the design and application of OSM-structured ReRAM in memory technologies.

Acknowledgements

Project supported in part by the National Natural Science Foundation of China (Grant Nos. 51602160 and 61605086), the Natural Science Foundation of Jiangsu Province, China (Grant No. BK20150842), the Talent Project of Nanjing University of Posts and Telecommunications (NUPTSF) (Grant No. NY222127).

References

[1] Wong H S P and Salahuddin S 2015 *Nat. Nanotech.* **10** 191
[2] Waser R, Dittmann R, Staikov G and Szot K 2009 *Adv. Mater.* **21** 2632
[3] Ielmini D 2016 *Semicond. Sci. Technol.* **31** 063002
[4] Zahoor F, Nisar A, Bature U I, Abbas H, Bashir F, Chattopadhyay A, Kaushik B K, Alzahrani A and Hussin F A 2024 *Nanoscale Adv.* **6** 4980
[5] Yang Y, Zhao J, Liu Y, Hua X, Wang T, Zheng J, Hao Z, Xiong B, Sun C, Han Y, Wang J, Li H, Wang L and Luo Y 2024 *Chin. Phys. B* **33** 030702
[6] Wang Z, Wu H, Burr G W, Hwang C S, Wang K L, Xia Q and Yang J J 2020 *Nat. Rev. Mater.* **5** 173
[7] Chen S and Valov I 2022 *Adv. Mater.* **34** 2105022
[8] Rehman M M, Yang B S, Yang Y J, Karimov K S and Choi K H 2017 *Curr. Appl. Phys.* **17** 533
[9] Sawa A 2008 *Mater. Today* **11** 28
[10] Munir F, Schön D, Menzel S, Stasner P, Waser R and Wiefels S 2024 *IEEE Trans. Electron Dev.* **71** 6691
[11] Yang J J, Strukov D B and Stewart D R 2013 *Nat. Nanotechnol.* **8** 13
[12] Pan F, Gao S, Chen C, Song C and Zeng F 2014 *Mater. Sci. Eng. R Rep.* **83** 1
[13] Zhang W, Lei J, Dai Y, Zhang X, Kang L, Peng B and Hu F 2022 *Nanotechnology* **33** 255703
[14] Jiang Z, Zhang W, Bao J, Cheng H, Zhang X and Hu F 2020 *Ceram. Int.* **46** 24838
[15] Hsu C C, Wang T C and Tsao C C 2018 *J. Alloys Compd.* **769** 65
[16] Tsai T L, Chang H Y, Lou J J C and Tseng T Y 2016 *Appl. Phys. Lett.* **108** 153505
[17] Li Y, Long S, Zhang M, Liu Q, Shao L, Zhang S, Wang Y, Zuo Q, Liu S and Liu M 2010 *IEEE Electron Dev. Lett.* **31** 117
[18] Lee J, Bourim E M, Lee W and Hwang H 2010 *Appl. Phys. Lett.* **97** 172105
[19] Kamata Y, Kamimuta Y, Ino T, Nabatame T and Torii K 2005 *Jpn. J. Appl. Phys.* **44** 2323
[20] Lee S, Kim T, Jang B, Lee W, Song K C, Kim H S, Do G Y, Hwang S B, Chung S and Jang J 2018 *IEEE Electron Dev. Lett.* **39** 668
[21] Wang S Y, Lee D Y, Huang T Y, Wu J W and Tseng T Y 2010 *Nanotechnology* **21** 495201
[22] Wong H S P, Lee H Y, Yu S, Chen Y S, Wu Y, Chen P S, Lee B, Chen F T and Tsai M J 2012 *Proc. IEEE* **100** 1951
[23] Huang X, Wang Y, Huang H, Duan L and Guo T 2024 *Chin. Phys. B* **33** 017303

[24] Li Y, Long S, Lv H, Liu Q, Wang Y, Zhang S, Lian W, Wang M, Zhang K, Xie H, Liu S and Liu M 2011 *Nanotechnology* **22** 254028
[25] Liu H C, Tang X G, Liu Q X, Jiang Y P, Li W H, Guo X B and Tang Z H 2020 *Ceram. Int.* **46** 21196
[26] Choi K and Pak J J 2024 *Semicond. Sci. Technol.* **39** 045012
[27] Jang B, Kim J, Lee J, Jang J and Kwon H 2024 *J. Mater. Sci. Technol.* **189** 68
[28] Marikkannan M, Subramanian M, Mayandi J, Tanemura M, Vishnukanthan V and Pearce J M 2015 *AIP Adv.* **5** 017128
[29] Marchewka A, Roesgen B, Skaja K Skaja K, Du H, Jia C L, Mayer J, Rana V, Waser R and Menzel S 2016 *Adv. Electron. Mater.* **2** 1500233
[30] Zhang W, Guo Z, Dai Y, Lei J, Wang J and Hu F 2023 *Ceram. Int.* **49** 35973
[31] Huang Y, Shen Z, Wu Y, Xie M, Hu Y, Zhang S, Shi X and Zeng H 2016 *AIP Adv.* **6** 025018
[32] Saitoh S and Kinoshita K 2020 *Appl. Phys. Lett.* **116** 112101
[33] Wang X, Sun B, Li X, Guo B, Zeng Y, Mao S, Zhu S, Xia Y, Tian S and Luo W 2018 *Ceram. Int.* **44** 18108
[34] Ismail M, Abbas H, Choi C and Kim S 2020 *J. Alloys Compd.* **835** 155256
[35] Ali S, Hussain M, Ismail M, Iqbal M W and Kim S 2024 *J. Alloys Compd.* **997** 174802
[36] Lata L K and Jain P K 2023 *Emergent Mater.* **6** 1979
[37] Zhang W, Ouyang J, Kang L M, Cheng H B, Yang Q and Hu F R 2015 *J. Mater. Sci.: Mater. Electron.* **26** 9962
[38] Kim W, Menzel S, Wouters D J, Waser R and Rana V 2016 *IEEE Electron Dev. Lett.* **37** 564
[39] Zhang W, Peng B, Kang L, Hu F, Cheng H and Wang Y 2022 *Mater. Res. Bull.* **145** 111553